Supplementary Information for

Massive coastal permafrost erosion during the Bølling-Allerød warm period

Alessio Nogarotto* *et al.*

*Corresponding author. Email: alessio.nogarotto@unive.it

This Supplementary Material file includes:

Supplementary methods
Figures S1 to S7
Tables S1 to S2
Supplementary references

Supplementary methods

Subsampling and sample handling

HH11-09 gravity core (GC) was subsampled at 2-cm resolution at the University Centre in Svalbard (UNIS). Humid samples were packaged in isolated plastic bags and shipped via courier to the laboratories of the Institute of Polar Sciences in Bologna, Italy. Since the shipment took longer than expected, after arrival 5 random intervals were selected to check for potential degradation and/or contamination during the shipment. Their analyses were compared to the same 5 intervals shipped via passenger flights (less than 2-day travel), revealing no loss of organic content or degradation took place.

Calculation of indexes

Lignin is an organic macromolecule abundant in all types of vascular plants. Upon alkaline CuO oxidation (see Materials and Methods), lignin yields 8 main products, divided in vanillyl, syringyl and cinnamyl phenols: vanillin (Vl), acetovanillone (Vn), vanillic acid (Vd), syringealdehyde (Sl), acetosyringone (Sn), syringic acid (Sd), p-coumaric acid (pCd), ferulic acid (Fd). The sum of these products, also called Λ or Λ-8, represents the total lignin content of the sample. The different ratios of lignin phenols that characterize a sample can indicate different types of vegetation, degree of degradation, contribution from pollen, and other useful insights on the composition of the biospheric material[1,2].

Cutin is a biopolymer and an important constituent of vascular plant cuticles, often used to estimate the terrestrial contribution in sediments together with lignin[2]. Upon alkaline CuO oxidation (see Materials and Methods), cutin yields 8 main products: 16-hydroxyhexadecanoic acid (ω-C16), hexadecan-1,16-dioic acid (C16DA), 18-hydroxyoctadec-9-enoic acid (ω-C18:1), 7 or 8-dihydroxy C_{16} α,ω-dioic acid (x-OH-C16DA) and 8, 9 or 10 16-dihydroxy C_{16} acids (x,ω-OH-C16). The sum of these acids represents the total cutin content of the sample.

The Carbon Preference Index (CPI; Equation 1) and the Average Chain Length (ACL; Equation 2) of *n*-alkanes represents, respectively, the ratio between odd over even carbon chain length molecules and the average number of carbon atoms they have. Since terrestrial vascular plants produce a range of *n*-alkanes with a strong odd-over-even signal and show only a couple of

dominant chain lengths[3,4], they are commonly used, in the marine environment, as proxies for terrestrial biospheric contribution.

Equation 1[5]

$$CPI = \frac{1}{2}\left(\frac{C25 + C27 + C29 + C31}{C24 + C26 + C28 + C30} + \frac{C25 + C27 + C29 + C31}{C26 + C28 + C30 + C32}\right)$$

Equation 2[6]

$$ACL = \frac{\sum_{n=15}^{35} Cn * n}{\sum_{n=15}^{35} Cn}$$

Tetraunsaturated alkenones are usually associated with freshwater environments[7–9] and they are commonly reported by means of their relative abundances in their group[9,10]. In our work, we also decided to report them as relative abundances for two main reasons: (a) in order to allow better comparison with other studies; and (b) because in the case of methyl C_{38} alkenones we could not convert SIM chromatographic results to TIC peak areas, thus preventing us from quantifying their actual concentrations.

Equation 3

$$\%MeC37{:}4 = 100 * \frac{MeC37{:}4}{MeC37{:}2 + MeC37{:}3 + MeC37{:}4}$$

Equation 4

$$\%MeC38{:}4 = 100 * \frac{MeC38{:}4}{MeC38{:}2 + MeC38{:}3 + MeC38{:}4}$$

Compound specific radiocarbon ages processing

The method proposed in Schefuß *et al.*[11] and Winterfeld *et al.*[12] was used to extrapolate pre-depositional ages of FAME compound. $\Delta^{14}C$ values measured and reported in Supplementary Table 2 were used to calculate the $\Delta^{14}C$ at the time of deposition ($\Delta^{14}C_{initial}$):

Equation 5

$$\Delta^{14}C_{initial} = \left[\left(\frac{\Delta^{14}C}{1000} + 1\right) * e^{\lambda t} - 1\right] * 1000$$

Where $\lambda=1/8267\ y^{-1}$ and t is the time of deposition of the sediment interval from the age-depth model.

Pre-depositional ^{14}C ages were calculated with the formula:

Equation 6

$$age = -8033 * ln\left(\frac{1+\frac{\Delta^{14}C_{initial}}{1000}}{1+\frac{\Delta^{14}C_{atm}}{1000}}\right)$$

Where $\Delta^{14}C_{atm}$ is the atmospheric $\Delta^{14}C$ at the time of deposition estimated from the IntCal20 dataset[13] and from direct measurement[14] for the top (modern) sample. Gaussian error propagation (http://www.julianibus.de/) was used to estimate the uncertainty on the derived pre-depositional ages from the initial errors on $\Delta^{14}C$, time of deposition (from the age-depth model) and $\Delta^{14}C_{atm}$. Out of the initial 24 radiocarbon datings obtained on individual FAMEs, 5 results were too close to the radiocarbon dating limit (approximately 50000 years) and with too large uncertainties to calculate pre-depositional ages.

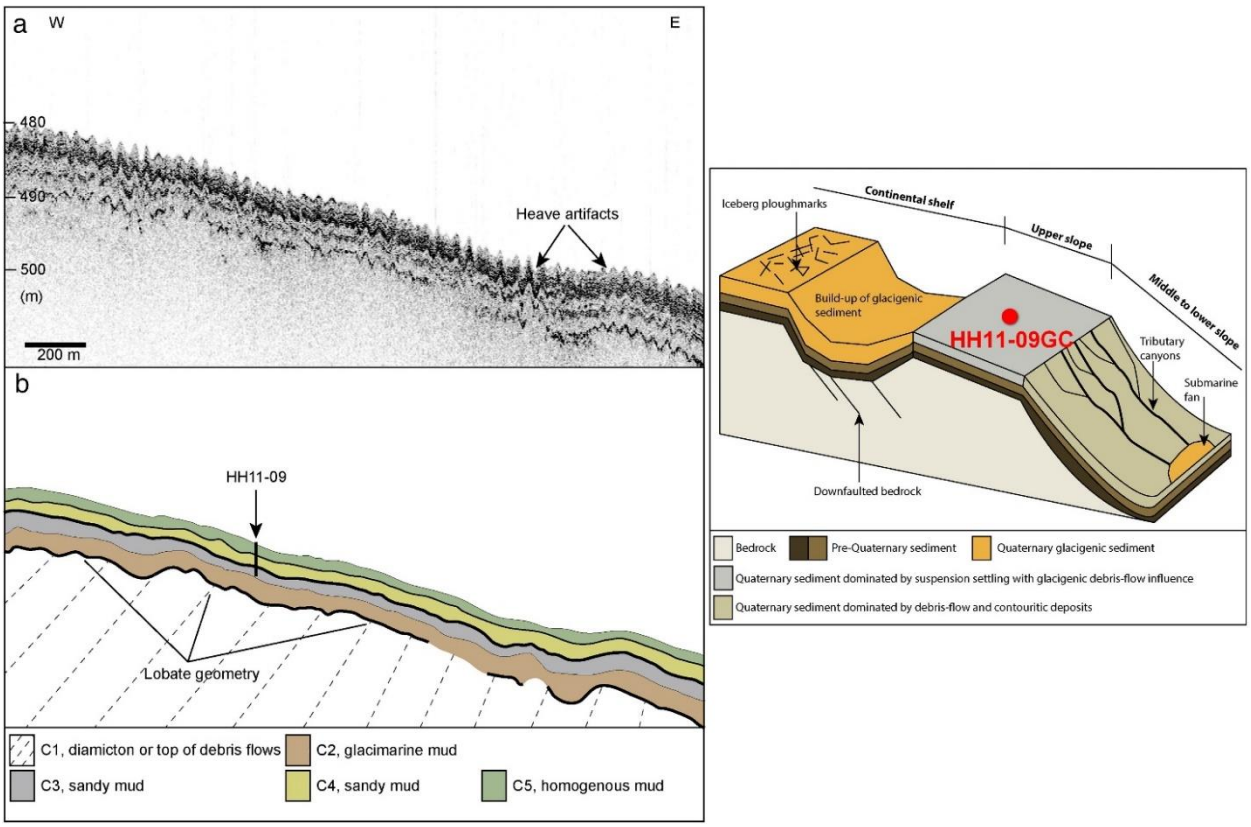

Fig. S1. Sub-bottom profile of the core location. (a) Chirp profile along the upper slope of Albertini trough with (b) interpreted sub-parallel reflectors, showing the location and approximate penetration of HH11-09GC sediment core[15]. (c) Illustrated sketch of distal continental shelf and slope in front of Albertini trough, showing the approximate position of the core. The presence of down-faulted bedrock before the upper slope is thought to be the primary reason of the absence of a trough mouth fan and of important glacial-related deposits for most of the last glacial period and deglaciation on the upper slope. Images slightly modified from Fransner *et al.*[16].

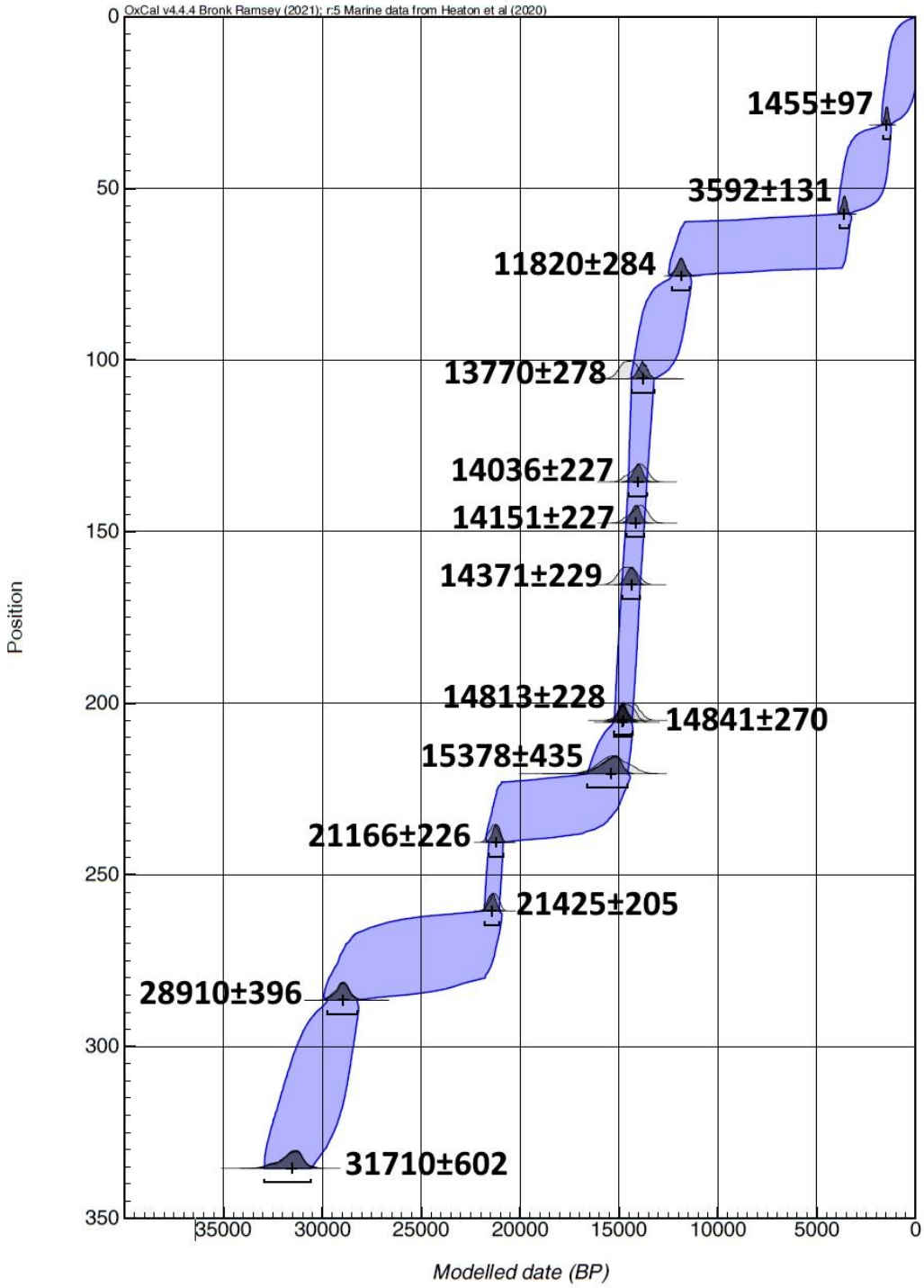

Fig. S2. Age-depth model. Graphical representation of the Bayesian age-depth model realized with OxCal 4.4.4[17]. The median of the 14 modelled datings used to build the model are reported, with 1σ uncertainty, beside their plotted statistical distribution.

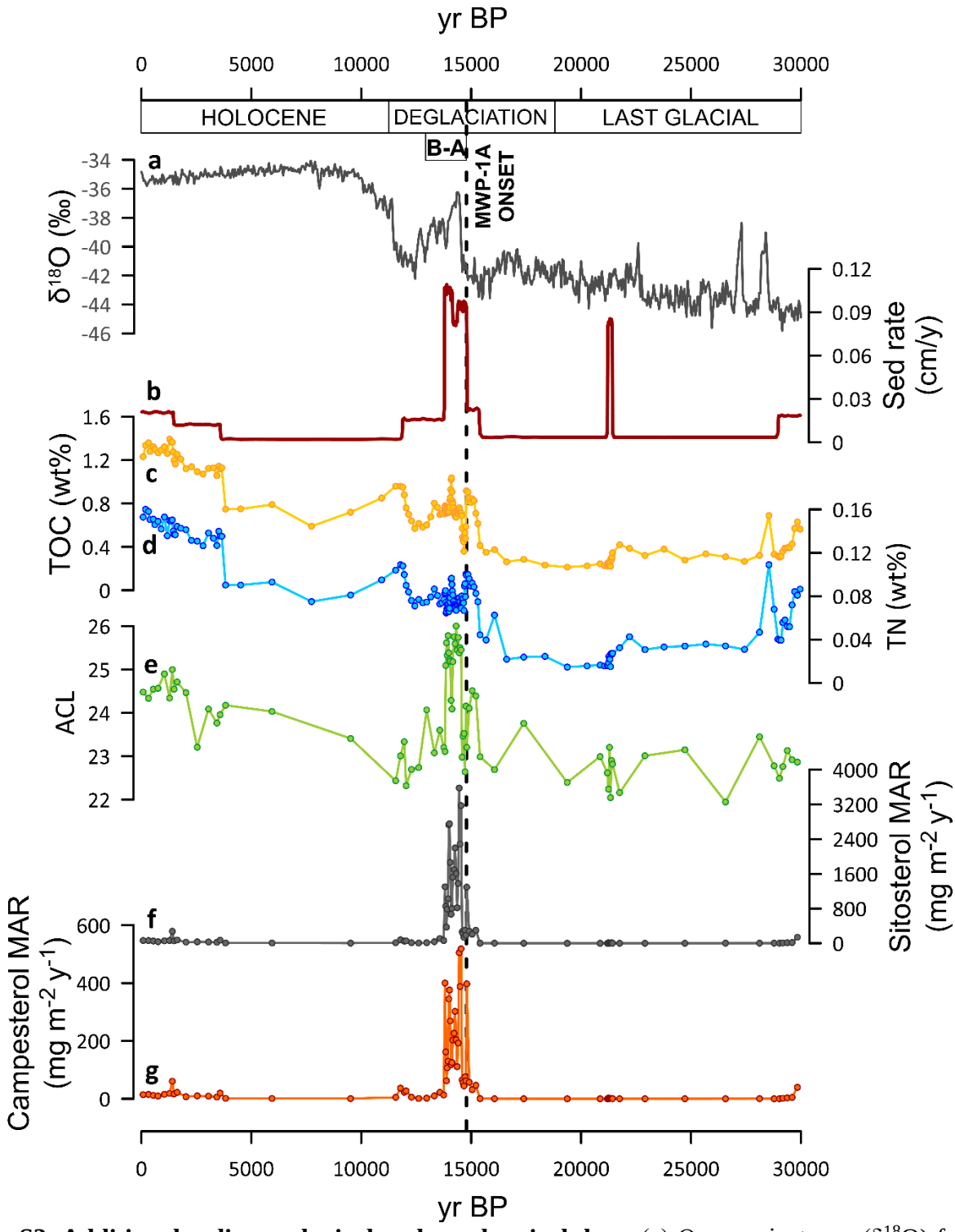

Fig. S3. Additional sedimentological and geochemical data. (a) Oxygen isotopes ($\delta^{18}O$) from Greenland ice cores[18] (black line); (b) Modelled sedimentation rate in the core location derived from the age-depth model calculation on OxCal (red line); (c) Total organic carbon (TOC, yellow line and dots) and (d) nitrogen (TN, blue line and dots); (e) Average Chain Length (ACL, green line and dots) of *n*-alkanes; (f) Sitosterol (grey line and dots) and (g) campesterol (orange line and dots) mass accumulation rates (MAR). The vertical dashed line displays the onset of MWP-1A.

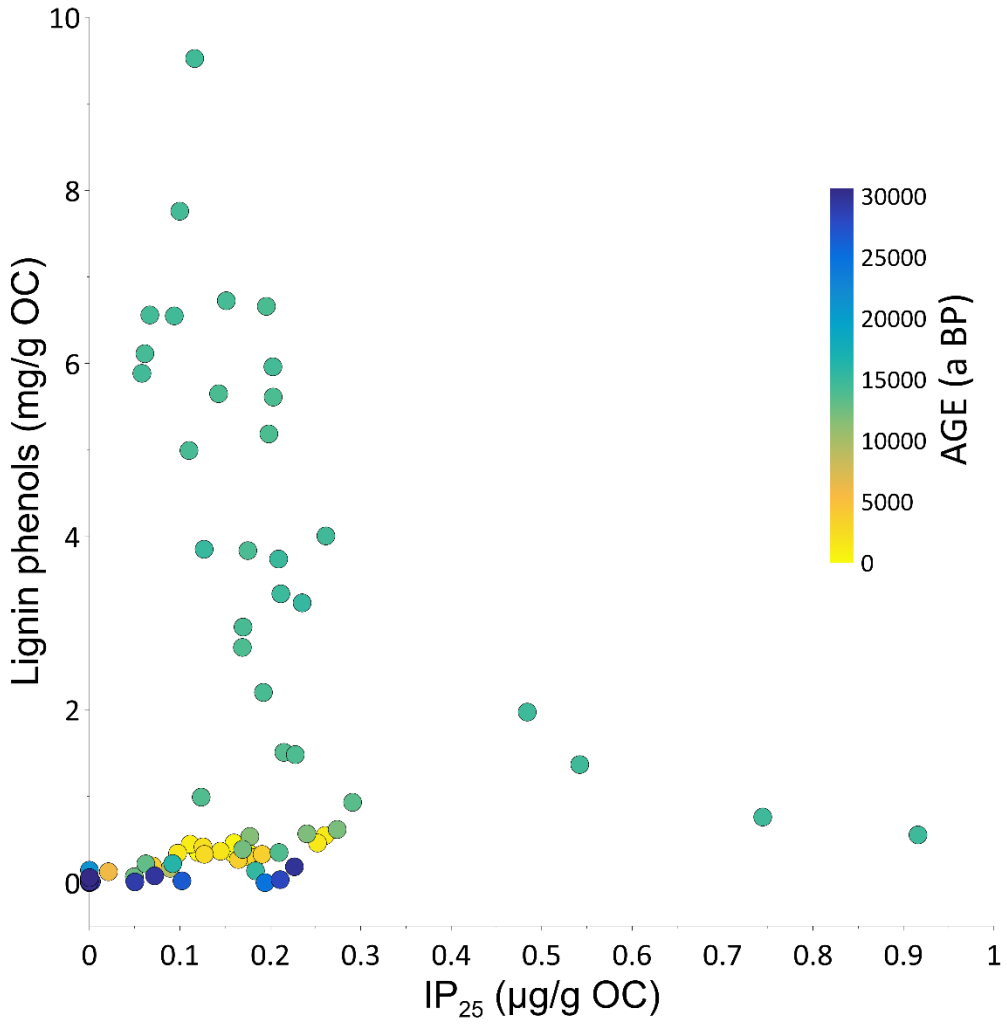

Fig. S4. Correlation between sea ice proxy and terrestrial biomarkers. Horizontal axis represents the concentration of the sea ice proxy IP_{25} and the vertical axis represents the concentration of lignin phenols, both normalized for the OC content. The color of the circles changes with the age of sedimentation.

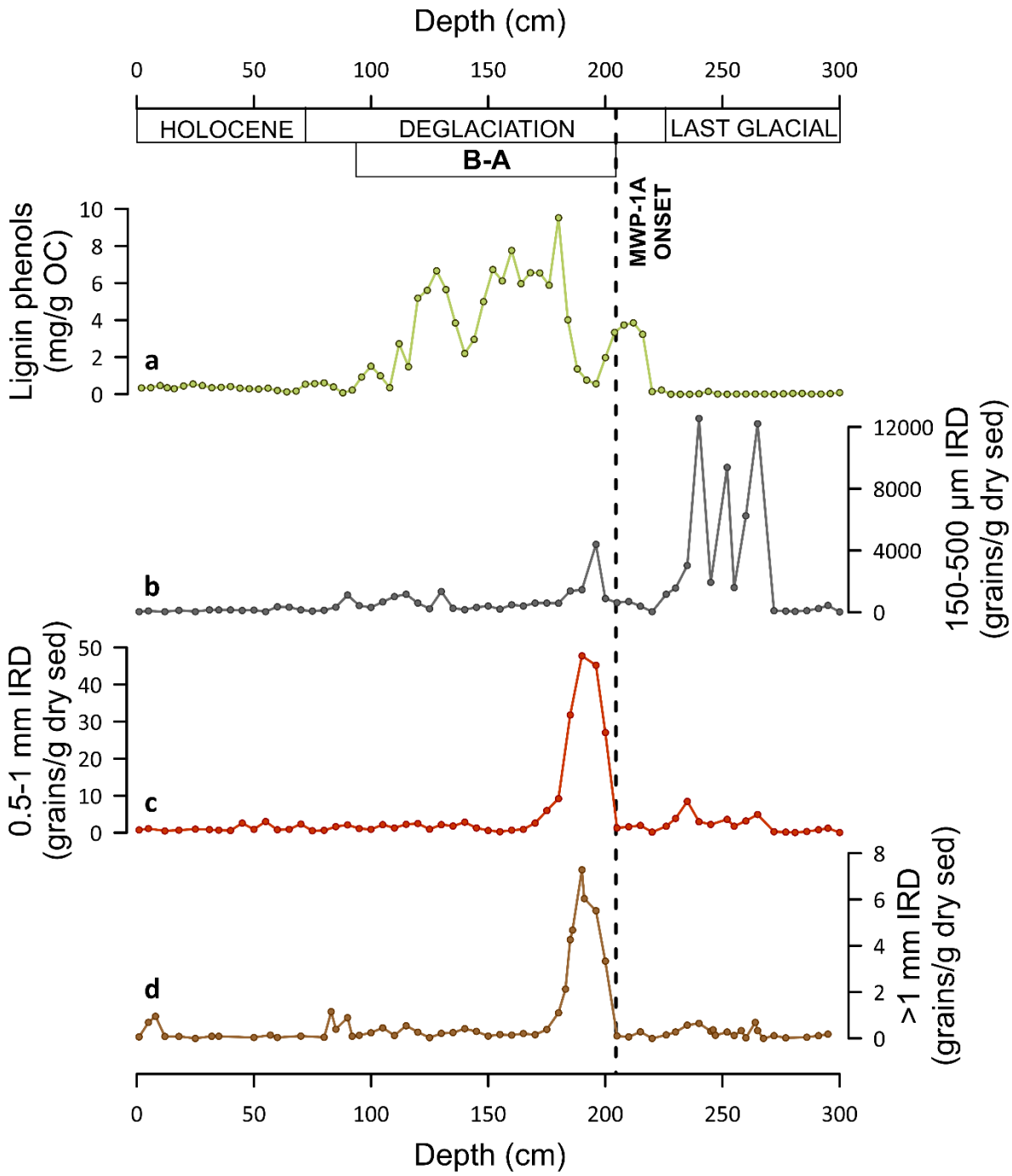

Fig. S5. Additional sedimentological data. (a) Lignin phenols (green line and dots) concentration (OC-normalized); (b) 150-500µm (grey line and dots), (c) 0.5-1mm (red line and dots) and (d) >1mm (brown line and dots) ice rafted debris (IRD) distribution. IRD data from Chauhan *et al.*[19]**.** The vertical dashed line displays the onset of MWP-1A.

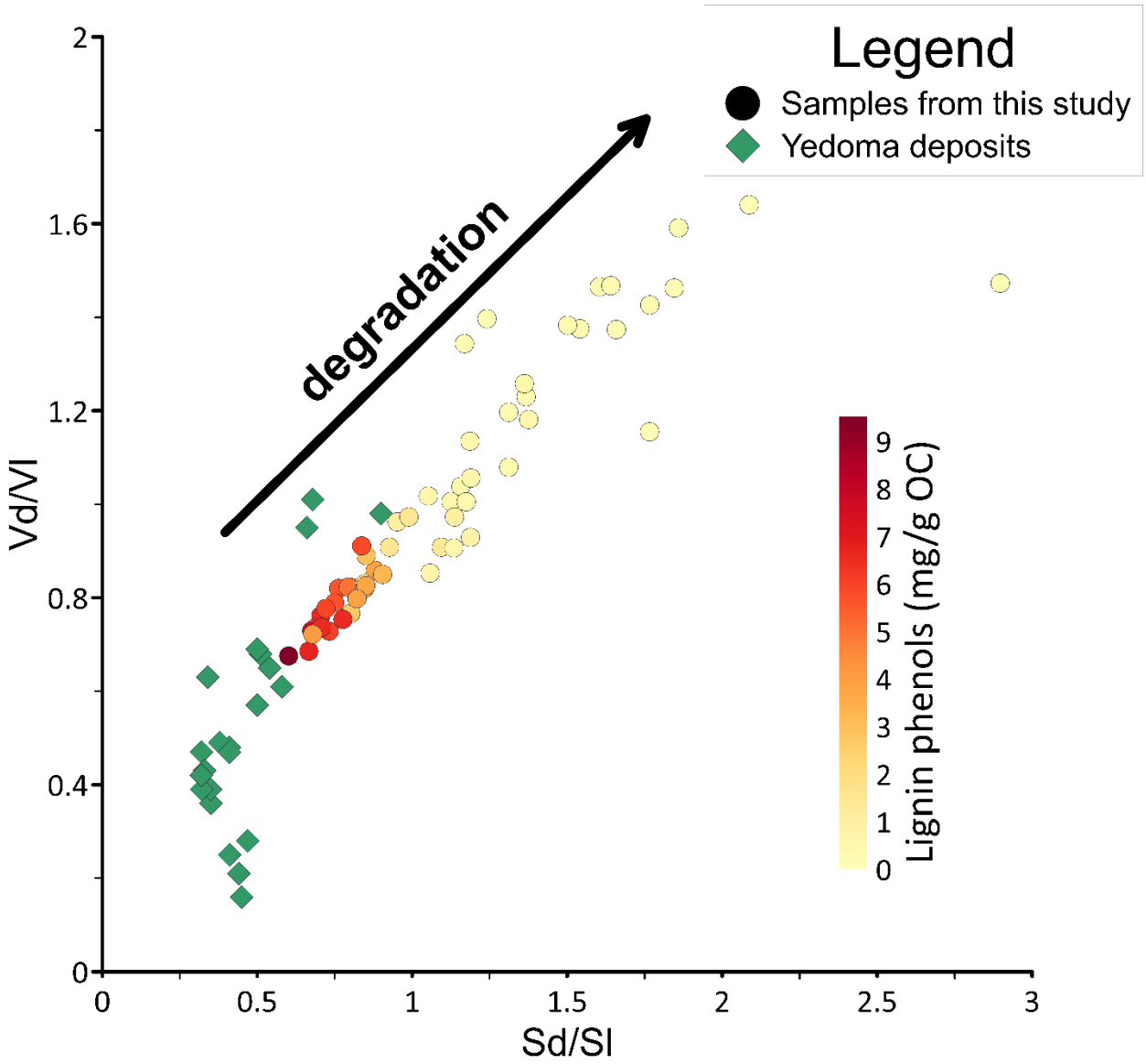

Fig. S6. Lignin degradation proxies. The graph shows the relation between acid to aldehyde ratio of syringyl (Sd/Sl) and vanillyl (Vd/Vl) phenols. Filled circles represent samples from core HH11-09GC, with filling color depending on the total lignin phenols concentration. For comparison, data from ice complex deposits (Yedoma)[2] are represented as green diamonds.

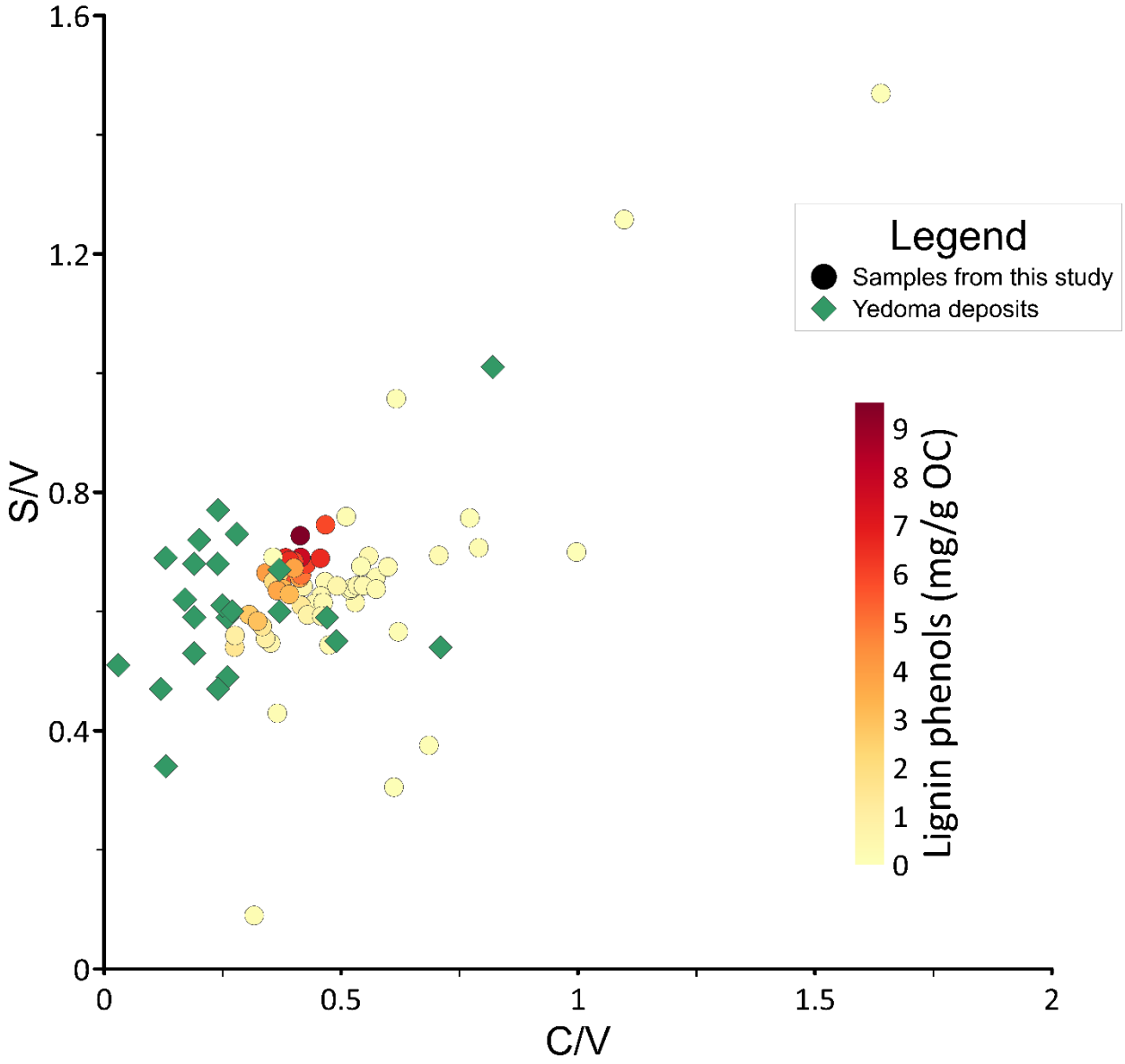

Fig. S7. Lignin source proxies. The graph shows the relation between cinnamyl over vanillyl (C/V) and syringyl over vanillyl (S/V) phenols ratio. Filled circles represent samples from core HH11-09GC, with filling color depending on the total lignin phenols concentration. For comparison, data from ice complex deposits (Yedoma)[2] are represented as green diamonds.

Facility	ID	Ref	Depth (cm)	Sample type	AMS ^{14}C age (yr)	σ ^{14}C age (yr)	ΔR (yr)	σ ΔR (yr)	ΔR ref	Modelled age (yr BP)	σ modelled age (yr)
Lund Radiocarbon Dating Laboratory	LuS10822	1	31	Mixed planthic foraminifera	2010	45	-55	35	1	1455	97
Lund Radiocarbon Dating Laboratory	LuS10823	1	57	Mixed planthic foraminifera	3770	65	-55	35	1	3592	131
Lund Radiocarbon Dating Laboratory	LuS10824	1	75	Mixed benthic foraminifera	10610	70	-80	95	2	11820	284
AWI-MICADAS	8336.1.1	2	105	Mixed benthic foraminifera	13094	124	230	250	2	13770	278
AWI-MICADAS	8337.1.1	2	135	Mixed benthic foraminifera	12616	127	110	260	2	14036	227
AWI-MICADAS	8338.1.1	2	147	Mixed benthic foraminifera	12564	128	70	260	2	14151	227
Lund Radiocarbon Dating Laboratory	LuS10825	1	165	Mixed benthic foraminifera	13270	70	358	285	2	14371	229
AWI-MICADAS	8339.1.1	2	205	Mixed benthic foraminifera	12972	128	132	260	2	14813	228
NOSAMS	OS-163812	2	206	Mixed benthic foraminifera	13350	100	420	200	2	14841	270
Ångstrom Radiocarbon Laboratory	Ua-46353	1	220	Bivalve	14382	488	970	125	2	15378	435
Lund Radiocarbon Dating Laboratory	LuS10826	1	240	*N. pachyderma*	18565	85	170	100	2	21166	226
Lund Radiocarbon Dating Laboratory	LuS10827	1	260	*N. pachyderma*	18545	85	170	100	2	21425	205
Lund Radiocarbon Dating Laboratory	LuS10828	1	286	Mixed benthic foraminifera	25800	300	170	100	2	28910	396
Lund Radiocarbon Dating Laboratory	LuS10830	1	335	*N. pachyderma*	28350	500	170	100	2	31710	602

Table S1. List of radiocarbon datings used in the realization of the age-depth model with their respective ΔR. Ref 1: Chauhan et al. (2016)[19]. Ref 2: this study. ΔR ref 1: Heaton et al. (2020)[20]. ΔR ref 2: Brendryen et al. (2020)[21].

Depth (cm)	Individual FAME	AMS ^{14}C AGE (yr)	σ AMS ^{14}C AGE (yr)	$\Delta^{14}C$ (‰)	σ $\Delta^{14}C$ (‰)	Sedimentation age (yr BP)	σ sedimentation age (yr)	$\Delta^{14}C_{initial}$ (‰)	σ $\Delta^{14}C_{initial}$ (‰)	Pre-depositional ^{14}C age (yr)	σ pre-depositional ^{14}C age (yr)
0-2	$C_{24:0}$	5586	271	-496.8	17.3	-59	156	-500.4	19.6	5931.4	314.6
0-2	$C_{26:0}$	4635	209	-433.6	14.9	-59	156	-437.6	18.2	4980.6	260.3
39-41	$C_{24:0}$	8524	311	-651.0	13.8	1965	670	-557.3	39.9	6444.0	724.2
39-41	$C_{26:0}$	7551	228	-606.0	11.3	1965	670	-500.3	43.0	5470.9	690.9
39-41	$C_{28:0}$	12294	895	-781.7	25.7	1965	670	-723.1	39.6	10214.2	1149.1
77-80	$C_{24:0}$	20696	1096	-923.3	11.2	11958	410	-674.1	50.3	10351.0	1240.5
77-80	$C_{26:0}$	20948	1163	-925.7	11.6	11958	410	-684.2	51.6	10603.3	1313.1
77-80	$C_{28:0}$	22059	2178	-935.3	20.2	11958	410	-725.0	86.7	11714.4	2533.8
125-130	$C_{24:0}$	31037	1377	-978.8	4.0	13973	253	-885.2	21.7	18966.0	1522.0
125-130	$C_{26:0}$	33433	1753	-984.3	3.8	13973	253	-914.8	20.9	21362.2	1974.2
125-130	$C_{28:0}$	45833	6627	-996.6	4.3	13973	253	/	/	/	/
137-141	$C_{24:0}$	32009	1620	-981.2	4.2	14073	232	-897.1	23.2	20274.4	1809.5
137-141	$C_{26:0}$	39745	3864	-992.8	4.4	14073	232	-960.7	24.3	28010.4	4966.7
137-141	$C_{28:0}$	43951	6172	-995.8	4.9	14073	232	/	/	/	/
159-161	$C_{24:0}$	33003	1586	-983.4	3.6	14309	237	-906.4	20.6	20581.8	1769.7
159-161	$C_{26:0}$	35455	2289	-987.8	4.0	14309	237	-931.0	22.8	23034.1	2659.0
159-161	$C_{28:0}$	42360	4999	-994.8	4.5	14309	237	-971.3	24.8	30076.5	6939.0
178-182	$C_{24:0}$	48679	8305	-997.6	4.3	14536	242	/	/	/	/
178-182	$C_{26:0}$	36090	2314	-988.7	3.8	14536	242	-934.5	22.0	23582.6	2692.6
178-182	$C_{28:0}$	61491	19062	-999.5	4.6	14536	242	/	/	/	/
178-182	$C_{30:0}$	47527	8553	-997.3	5.2	14536	242	/	/	/	/
211-213	$C_{24:0}$	34660	2348	-986.5	4.6	15027	429	-917.0	28.5	21977.4	2758.9
211-213	$C_{26:0}$	31958	1613	-981.1	4.2	15027	429	-883.8	26.5	19275.5	1834.8
211-213	$C_{28:0}$	38010	3499	-991.1	4.9	15027	429	-945.3	30.0	25327.8	4405.4

Table S2. List of compound specific radiocarbon datings (CSRA). No pre-depositional ages are shown for 5 samples which are too close to the limit of radiocarbon dating ($\Delta^{14}C < -995‰$).

Supplementary references

1. Goñi, M. A. & Hedges, J. I. Lignin dimers: Structures, distribution, and potential geochemical applications. *Geochim Cosmochim Acta* **56**, 4025–4043 (1992).
2. Tesi, T. *et al.* Composition and fate of terrigenous organic matter along the Arctic land-ocean continuum in East Siberia: Insights from biomarkers and carbon isotopes. *Geochim Cosmochim Acta* **133**, 235–256 (2014).
3. Eglinton, G. & Hamilton, R. J. Leaf Epicuticular Waxes. *Science (1979)* **156**, 1322–1335 (1967).
4. Eglinton, G. & Hamilton, R. J. The Distribution of Alkanes. in *Chemical Plant Taxonomy* (ed. Swain, T.) vol. 8 187–217 (Academic Press, 1963).
5. Bray, E. E. & Evans, E. D. Distribution of n-paraffins as a clue to recognition of source beds. *Geochim Cosmochim Acta* **22**, 2–15 (1961).
6. Cranwell, P. A., Eglinton, G. & Robinson, N. Lipids of aquatic organisms as potential contributors to lacustrine sediments—II. *Org Geochem* **11**, 513–527 (1987).
7. Bendle, J., Rosell-Melé, A. & Ziveri, P. Variability of unusual distributions of alkenones in the surface waters of the Nordic seas. *Paleoceanography* **20**, 1–15 (2005).
8. Rosell-Melé, A., Jansen, E. & Weinelt, M. Appraisal of a molecular approach to infer variations in surface ocean freshwater inputs into the North Atlantic during the last glacial. *Glob Planet Change* **34**, 143–152 (2002).
9. Kaiser, J., van der Meer, M. T. J. & Arz, H. W. Long-chain alkenones in Baltic Sea surface sediments: New insights. *Org Geochem* **112**, 93–104 (2017).
10. Wang, K. J. *et al.* Group 2i Isochrysidales produce characteristic alkenones reflecting sea ice distribution. *Nat Commun* **12**, (2021).
11. Schefuß, E. *et al.* Hydrologic control of carbon cycling and aged carbon discharge in the Congo River basin. *Nat Geosci* **9**, 687–690 (2016).
12. Winterfeld, M. *et al.* Deglacial mobilization of pre-aged terrestrial carbon from degrading permafrost. *Nat Commun* **9**, (2018).
13. Reimer, P. J. *et al.* The IntCal20 Northern Hemisphere Radiocarbon Age Calibration Curve (0–55 cal kBP). *Radiocarbon* **62**, 725–757 (2020).
14. Levin, I., Kromer, B. & Hammer, S. Atmospheric Δ14CO2 trend in Western European background air from 2000 to 2012. *Tellus B: Chemical and Physical Meteorology* **65**, 20092 (2013).
15. Chauhan, T., Noormets, R. & Rasmussen, T. L. Glaciomarine sedimentation and bottom current activity on the north-western and northern continental margins of Svalbard during the late Quaternary. *Geo-Marine Letters* **36**, 81–99 (2016).
16. Fransner, O., Noormets, R., Flink, A. E., Hogan, K. A. & Dowdeswell, J. A. Sedimentary processes on the continental slope off Kvitøya and Albertini troughs north of Nordaustlandet, Svalbard – The importance of structural-geological setting in trough-mouth fan development. *Mar Geol* **402**, 194–208 (2018).

17. Ramsey, C. B. Bayesian analysis of radiocarbon dates. *Radiocarbon* **51**, 337–360 (2009).
18. North Greenland Ice Core Project members. High-resolution record of Northern Hemisphere climate extending into the last interglacial period. *Nature* **431**, 147–151 (2004).
19. Chauhan, T., Rasmussen, T. L. & Noormets, R. Palaeoceanography of the Barents Sea continental margin, north of Nordaustlandet, Svalbard, during the last 74 ka. *Boreas* **45**, 76–99 (2016).
20. Heaton, T. J. *et al.* Marine20 - The Marine Radiocarbon Age Calibration Curve (0-55,000 cal BP). *Radiocarbon* **62**, 779–820 (2020).
21. Brendryen, J., Haflidason, H., Yokoyama, Y., Haaga, K. A. & Hannisdal, B. Eurasian Ice Sheet collapse was a major source of Meltwater Pulse 1A 14,600 years ago. *Nat Geosci* **13**, 363–368 (2020).